Managing photon flux in a miniaturized photoionization detector

Mackenzie Meyer,[1,a)] (iD) Xiaheng Huang,[1,2,b)] (iD) Xudong Fan,[2,c)] (iD) and Mark J. Kushner[1,d)] (iD)

AFFILIATIONS

[1]Electrical Engineering and Computer Science Department, University of Michigan, 1301 Beal Ave., Ann Arbor, Michigan 48109-2122, USA

[2]Biomedical Engineering Department, University of Michigan, 1101 Beal Ave., Ann Arbor, Michigan 48109-2110, USA

[a)]maemeyer@umich.edu
[b)]xiaheng@umich.edu
[c)]xsfan@umich.edu
[d)]**Author to whom correspondence should be addressed:** mjkush@umich.edu

ABSTRACT

Miniaturized photoionization detectors (PIDs) are used in conjunction with gas chromatography systems to detect volatile compounds in gases by collecting the current from the photoionized gas analytes. PIDs should be inexpensive and compatible with a wide range of analyte species. One such PID is based on the formation of a He plasma in a dielectric barrier discharge (DBD), which generates vacuum UV (VUV) photons from excited states of He to photoionize gas analytes. There are several design parameters that can be leveraged to increase the ionizing photon flux to gas analytes to increase the sensitivity of the PID. To that end, the methods to maximize the photon flux from a pulsed He plasma in a DBD-PID were investigated using a two-dimensional plasma hydrodynamics model. The ionizing photon flux originated from the resonance states of helium, He(3P) and He(2^1P), and from the dimer excimer He$_2$*. While the photon flux from the resonant states was modulated over the voltage pulse, the photon flux from He$_2$* persisted long after the voltage pulse passed. Several geometrical optimizations were investigated, such as using an array of pointed electrodes. However, increasing the capacitance of the dielectric enclosing the plasma chamber had the largest effect on increasing the VUV photon fluence to gas analytes.

I. INTRODUCTION

Photoionization detectors (PIDs) are widely used in gas chromatography (GC) devices, particularly, in field-deployable micro-GC (μGC) devices.[1] PIDs have demonstrated the detection of volatile organic compounds (VOCs) including benzene and toluene to levels as low as a few parts per billion (ppb).[1–4] PIDs rely on vacuum UV (VUV) photons to ionize the gas analytes flowing through the ionization chambers.[5] VUV lamps filled with low pressure Kr and Ar gas are commonly used to produce photons up to 10.6 and 11.7 eV, respectively. However, lamp-based VUV sources have a short lifetime due to VUV window degradation and gas leakage.[6] Generation of VUV photons can also occur through a dielectric barrier discharge (DBD) without a VUV window.[7–12] For the gas analytes whose ionization potentials are higher than 11.7 eV and cannot be ionized by

Kr or Ar lamps, photons generated through a He discharge plasma need to be used. VUV photon emission from a He plasma dominantly occurs from three states. Resonant radiation from He(3P) and He(2^1P) emits photons of 23 and 21.2 eV, respectively. VUV photons are also produced by broadband He$_2$* dissociation excimer emission, with energies ranging from 11.3 to 20.7 eV.[13] The high energy VUV photons produced in a He plasma can photoionize almost all analytes, including most molecular gases (N$_2$, O$_2$, H$_2$, H$_2$O) and essentially all organic compounds.

We have recently developed miniaturized He dielectric barrier discharge PIDs (HDBD-PIDs) for highly sensitive gas detectors that are microfabricated on silicon wafers and have a size of only a few squared centimeters.[10,11] A detection limit of pico-grams has been achieved for a broad range of gas analytes. To further optimize the performance of the HDBD-PID, the photon flux to the

analyte should be maximized. In this regard, there have been few investigations with the goal of understanding the plasma processes for producing the VUV photons and strategies for maximizing the photon flux to the analyte based on plasma properties. For the typical operating conditions of PIDs, the system is not saturated. That is, a linear increase in the photon fluence to the analyte during a current pulse will produce a linear increase in the ion current detected. In this paper, the results from a modeling investigation performed for an HDBD-PID developed by Li et al.[11] will be discussed to determine device parameters that have the greatest leverage for maximizing the photon fluence to the analyte gas. This investigation was performed using a two-dimensional (2D) plasma hydrodynamics model. Although this investigation is focused on the generic DBD geometry implemented by Li et al.,[11] the design principles are more generally applicable.

A description of the model, geometry, and reaction mechanism, including the photoionization reaction mechanism, is in Sec. II. The results for photon production in the base case are discussed in Sec. III. Dependencies of the photon fluence due to the capacitance of the dielectric and electrode configuration are discussed in Secs. IV and V. Concluding remarks are in Sec. VI.

II. DESCRIPTION OF MODEL

The miniaturized HDBD-PID investigated here is described in detail in Li et al.[11] The top view of the device is shown schematically in Fig. 1(a). The plasma is produced in He that flows into a chamber (called plasma chamber) formed by two parallel dielectric plates with metal electrodes (called plasma electrodes) in the plane of the figure. The electrodes that produce the plasma are not in contact with the plasma, being located on the top of the top dielectric and the bottom of the bottom dielectric. The typical dimensions of the PID plasma chamber are a few mm across and a few hundred micrometers in height. Etched-through silicon separates the dielectric on the top and bottom of the plasma. There is a small opening in the plasma chamber that allows the VUV photons generated by He plasma to enter the ionization chamber formed by the two collection electrodes. Analytes flow into the ionization chamber between the collection electrodes and are photoionized by the VUV photons produced in the plasma chamber. The resultant ions and electrons are collected by the biased collection electrodes to produce the sensing signal, shown in Fig. 1(b). The analyte flow rate (usually 1–2 ml/min) is controlled by the upstream gas chromatography device to achieve the best analyte separation performance. The He flow rate is controlled so that the He plasma can be generated with a relatively low excitation power or voltage while avoiding any plasma entering the ionization chamber, which would, otherwise, produce background noise in the signal. An example of the data produced by the gas chromatograph in tandem with a He plasma HDBD-PID is in Fig. 1(b).

The modeling platform nonPDPSIM was used to simulate the miniaturized PID plasma generation and is described in detail in Norberg et al.[14] Briefly, nonPDPSIM represents plasma hydrodynamics on an unstructured mesh. The coupled transport equations for charged species densities (ions, electrons), electric potential, and charge in or on materials are solved using an implicit
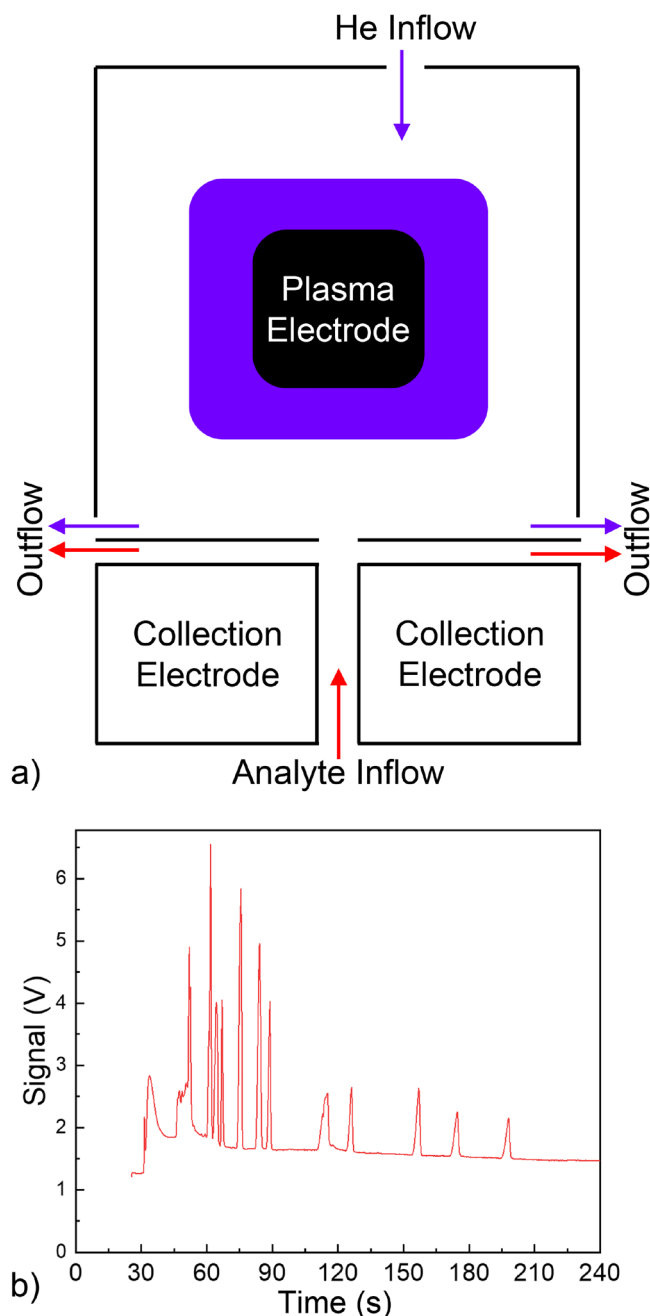

FIG. 1. Miniaturized HDBD-PID. (a) HDBD-PID schematic (top view), which includes both plasma generation chamber (or plasma chamber) and ionization chamber. (b) A chromatogram generated by the HDBD-PID in tandem with a 10 m long microfabricated GC column.

Newton–Raphson method. The electron temperature T_e is produced by integration of an electron energy equation. Rate coefficients for electron-impact processes are obtained from stationary solutions of Boltzmann's equation for the electron energy
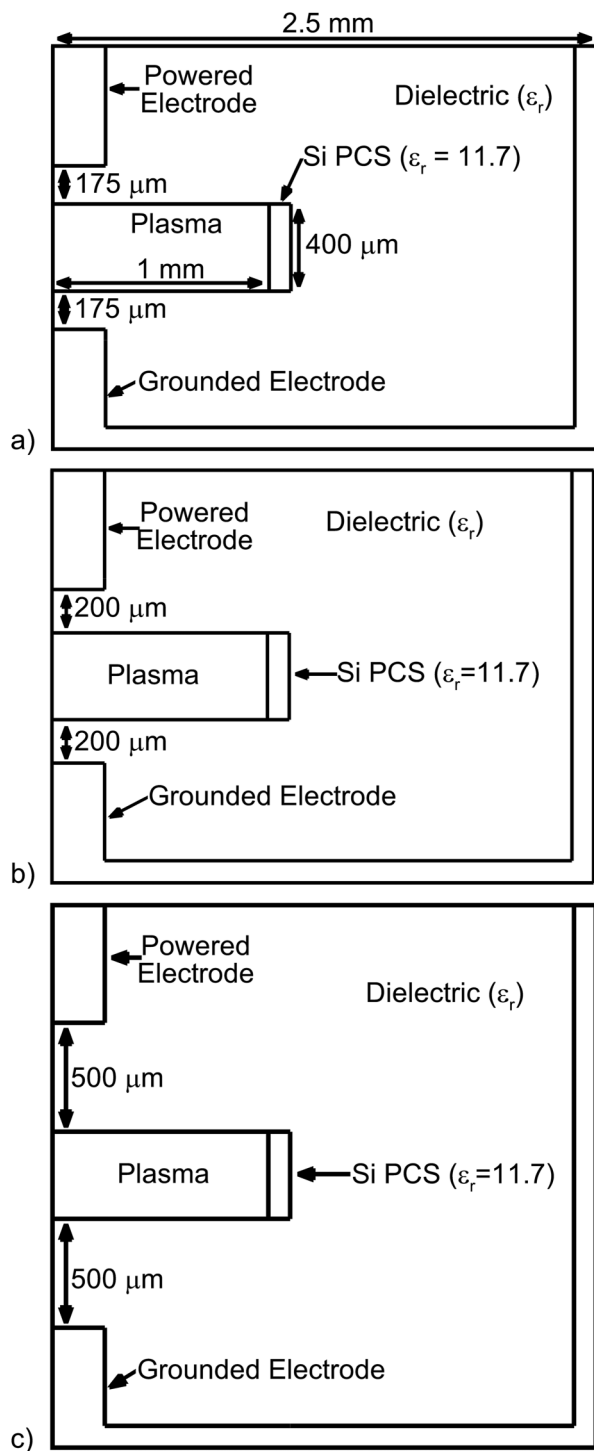
FIG. 2. Miniaturized HDBD-PID geometry modeled in *nonPDPSIM*. This geometry is a cross section of the HDBD-PID plasma generation chamber. (a) 175 µm thick dielectric, (b) 200 µm thick dielectric, and (c) 500 µm thick dielectric.

distributions. The neutral species densities are updated using their continuity equations accounting for transport and collisions. Radiation transport and photoionization are addressed using Green's function approach in which $G(\vec{r}, \vec{r}')$ represents the flux of isotropically emitted radiation originating at $\vec{r}$ that arrives at $\vec{r}'$ while accounting for absorption by plasma species and obscuration by intervening materials. The electron Monte Carlo simulation (eMCS), a module in *nonPDPSIM*, is used to track the secondary electron emission from the dielectric surfaces resulting from ion bombardment and photoelectron emission. The eMCS provides electron-impact source functions due to the secondary electrons and a source of secondary electrons to the bulk electrons.

A cross-section of the plasma in the miniaturized HDBD-PID was modeled, and the geometry for the base case is shown in Fig. 2(a). The plasma was formed in a 400 µm gap between the dielectric materials covering the grounded and powered electrodes. The dielectric thickness was 175 µm. A symmetric boundary condition was applied to the left boundary. Seed electrons and positive ions were initialized on the symmetric boundary underneath the powered electrode. The eMCS tracked the trajectory of secondary electrons extending 50 µm into the plasma from the top and bottom dielectric in contact with the plasma. The photon flux and fluence to the Si bounding the plasma gap were taken as the photon flux and fluence to the analyte inlet. This will be referred to below as the photon collecting surface (PCS). The numerical mesh had 14 808 total computational nodes with 11 516 nodes in the plasma. With the model being two-dimensional, the plasma properties are assumed to be uniform in the third dimension (perpendicular to the plane shown in Figs. 2–4).

The principle of operation of a DBD is based on dielectric materials covering one or both electrodes.[15] Current flowing to the dielectric surface(s) during a pulsed plasma charges the capacitance of the dielectric, which removes voltage from across the plasma gap. This removal of voltage from the plasma and charging of the dielectric(s) will terminate the discharge, which, in most cases, is the desired effect to prevent the arcing of the discharge. A discharge pulse whose voltage rapidly falls will discharge the capacitance of the dielectric(s) by producing a current pulse in the opposite direction, thereby enabling uni-polar pulses. Slowly varying sinusoidal voltages will discharge the voltage of the charged dielectric on the opposite polar portion of the cycle.

The capacitance C of the dielectric between the electrode and plasma determines the total charge transfer (time integrated current) through the plasma, the total energy deposition in the plasma, and so the photon fluence onto the PCS. C for a parallel plate capacitor is

$$C = \frac{\varepsilon_r \varepsilon_0 A}{d}, \qquad (1)$$

where ε_r is the relative permittivity of the dielectric, ε_0 is the permittivity of free space, A is the area of the dielectric in contact with the plasma, and d is the thickness of the dielectric. Although this expression is an approximation for more complex shapes, we will use Eq. (1) as a guide for how changes in materials and dimensions will affect photon production.

To investigate the consequences of capacitance on plasma properties and photon production, the geometries in Fig. 2 were
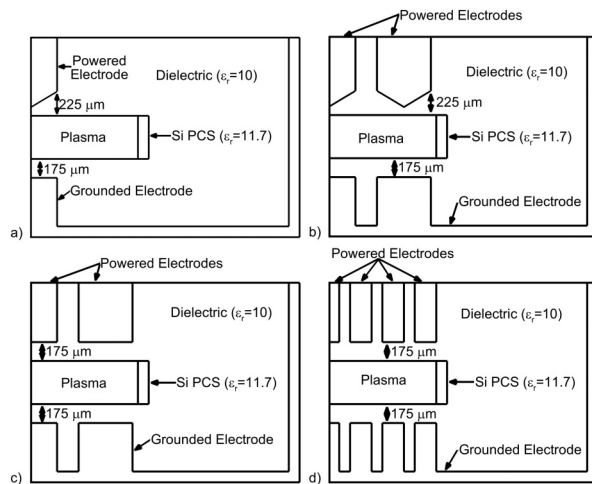
FIG. 3. Geometry for different electrode configurations. The images show half the computational domain, being symmetric across the left boundary. Electrodes on the axis are shown with half their width. (a) One pointed electrode, (b) three-pointed electrodes (one on the axis and two off-axis), (c) three flat electrodes, and (d) three flat electrodes (one on the axis, six off-axis).

FIG. 4. Full reactor geometry. (a) 1, (b) 0.75, (c) 0.5, and (d) 0.25 mm distance from the center of the electrode to the Si PCS.

used, varying the thickness of the dielectric (plasma to electrode) from 175 to 500 μm. The permittivity of the dielectric was selected based on viable microfabrication materials. The values considered were $\varepsilon_r = 10$ (sapphire, Al$_2$O$_3$), 85 (TiO$_2$), and 300 (SrTiO$_3$).

The electrode configuration can also be used to regulate the fluence to the PCS. Several electrode configurations were investigated, as shown in Fig. 3. The plasma facing surface of the powered electrode was varied from flat to pointed [Fig. 3(a)]. The dielectric between the plasma and powered electrode was 225 μm at its widest, decreasing to 75 μm at the narrowest point. The tapered electrode produces a large effective capacitance while also producing electric field enhancement. Adding additional powered electrodes allows for multiple plasma filaments to be sustained during a short discharge pulse [Figs. 3(b)–3(d)]. The images in Fig. 3 are for half the computational domain, being symmetric across the left boundary. For these simulations, plasma was seeded below each powered electrode.

The position of the electrode relative to the PCS also affects the photon fluence, if for no other reason than the solid angle subtended by the PCS relative to the plasma increases. That said, the location of the electrodes relative to other structures in the reactor affects the formation of the plasma. To examine the consequences of electrode location, the full reactor was modeled, as shown in Fig. 4. The geometry was essentially the same as in Fig. 2(a), except a symmetric boundary condition was no longer used. The electrodes were translated laterally across the plasma gap.

In all geometries, a −2 kV voltage pulse was applied to the powered electrode. The voltage pulse was 100 ns in length, with an additional 0.5 ns rise and fall time. The plasma was modeled for 150 ns to ensure that the decay of the voltage pulse was resolved.
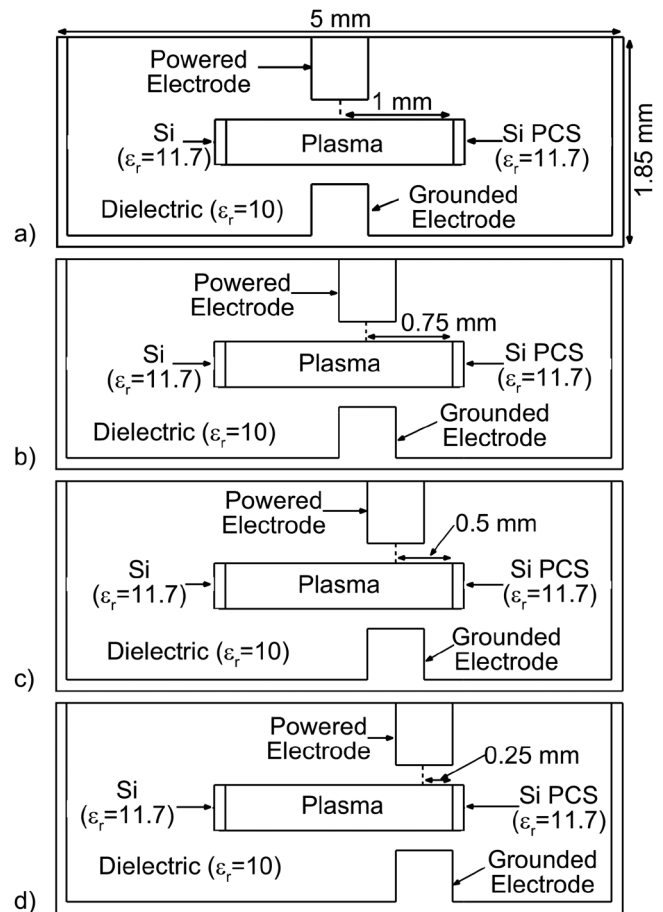
The simulated DBD was operated at atmospheric pressure in He with impurities of N$_2$ (80 ppm) and O$_2$ (20 ppm). The species included in the reaction mechanism are listed in Table I, totaling 31 species with 456 reactions. As N$_2$ and O$_2$ were present at an impurity level, higher order N$_x$O$_y$ species were not included. The reaction mechanism was based on Van Gaens and Bogaerts,[16] updated by Norberg to use He instead of Ar.[17] Further updates included branching ratios of recombination of He$^+$ and He$_2^+$ from Emmert et al.,[18]

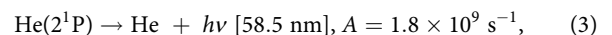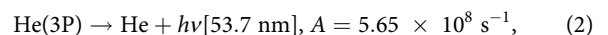Three photoemission reactions were included,

$$\text{He(3P)} \rightarrow \text{He} + h\nu[53.7 \text{ nm}], A = 5.65 \times 10^8 \text{ s}^{-1}, \quad (2)$$

$$\text{He(2}^1\text{P)} \rightarrow \text{He} + h\nu\,[58.5 \text{ nm}], A = 1.8 \times 10^9 \text{ s}^{-1}, \quad (3)$$

$$\text{He}_2^* \rightarrow \text{He} + \text{He} + h\nu[76 \text{ nm}], A = 10^7 \text{ s}^{-1}, \quad (4)$$

09 April 2024 11:30:17

TABLE I. Species included in the reaction mechanism.

e, He, He(2^3S), He(2^1S), He(2^3P), He(2^1P), He(3P), He(3S), He$^+$, He$_2^\star$, He$_2^+$

N$_2$, N$_2$(r), N$_2$(v), N$_2$(A$^3\Sigma_u$), N$_2$(a'$^1\Sigma$), N$_2^+$, N, N(^{2}D), N$^+$,

O$_2$, O$_2$(v), O$_2$(r), O$_2$($^1\Delta$), O$_2$($^1\Sigma$), O$_2^+$, O$_2^-$, O, O(^{1}D), O$^+$, O$^-$

where A is the rate of natural emission (inverse of the natural life-time). The broadband excimer radiation from He$_2^\star$ is centered at 76 nm while extending from 56 to 110 nm.[19] The natural lifetimes for the resonance transitions were adjusted for radiation trapping factors as calculated in Lietz et al.[20] The trapped emission rates were $A = 9.12 \times 10^5$ s^{-1} for He(3P) and $A = 2.0 \times 10^6$ s^{-1} for He (2^1P). The photons from each of these three photoemission reactions ionized N$_2$ with a cross section of 2.5×10^{-17} cm^2.[21] As this photoionization serves merely as a seed for propagation of the streamer, the photoionization of O$_2$ was not included as its contribution would be proportionally smaller. The flux and fluence of all species, including the photons, were collected on the Si PCS.

III. STREAMER PROPAGATION AND PHOTON FLUXES

The propagation of the filament of plasma (streamer) during the voltage pulse is shown in Fig. 5 for the geometry of the base case [Fig. 2(a) with $\varepsilon_r = 10$]. The electron density and electron-impact ionization source are shown. The ionization wave (IW) initially propagates from the top powered electrode toward the bottom grounded electrode in a Townsend mode. In this mode, the plasma density is not sufficient to produce large changes in the applied electric field, either through space charge or conductivity. Once the electrons reach the bottom of the plasma gap, the bottom dielectric is charged, which then launches a second IW, or restrike, toward the powered electrode (7 ns). This restrike is in the form of a true streamer with electric field enhancement at its leading edge. The electron temperature T_e is maximum in the head of the streamer initiating electron-impact ionization to continue propagation of the IW. At 17 ns, the electron density begins spreading on both the top and bottom dielectric surfaces as charge accumulates on the dielectric surfaces. This charge produces an electric field component parallel to the surface of the dielectric and enables the propagation of a surface ionization wave (SIW).

During the pulse (17, 27, 77 ns), the electron density remains high with a maximum value of 6×10^{14} cm^{-3}. While the electrons do recombine with positive ions during the pulse, electrons are also produced. One mechanism of electron production is the photoionization of N$_2$ from He$_2^\star$, He(2^1P), and He(3P). Penning ionization processes, where an excited He atom or He$_2^\star$ ionizes N$_2$ or O$_2$ (i.e., He* + N$_2 \rightarrow$ He + N$_2^+$ + e), also play a large role in sustaining the electron density during the pulse. As the voltage pulse falls (103 ns), a second reverse IW is launched, producing an increase in the electron density, simultaneous to launching secondary SIWs (103, 110 ns). The electron density remains high after the pulse (150 ns) due to photoionization and Penning ionization processes balancing the losses of electrons to recombination.

The simulated photon fluxes due to emission by He(3P), He(2^1P), and He$_2^\star$ are shown in Fig. 6 throughout the voltage

n_e (6×10^{14} cm^{-3}, 3 dec log) S_e (2×10^{22} cm^{-3}s^{-1}, 4 dec log)
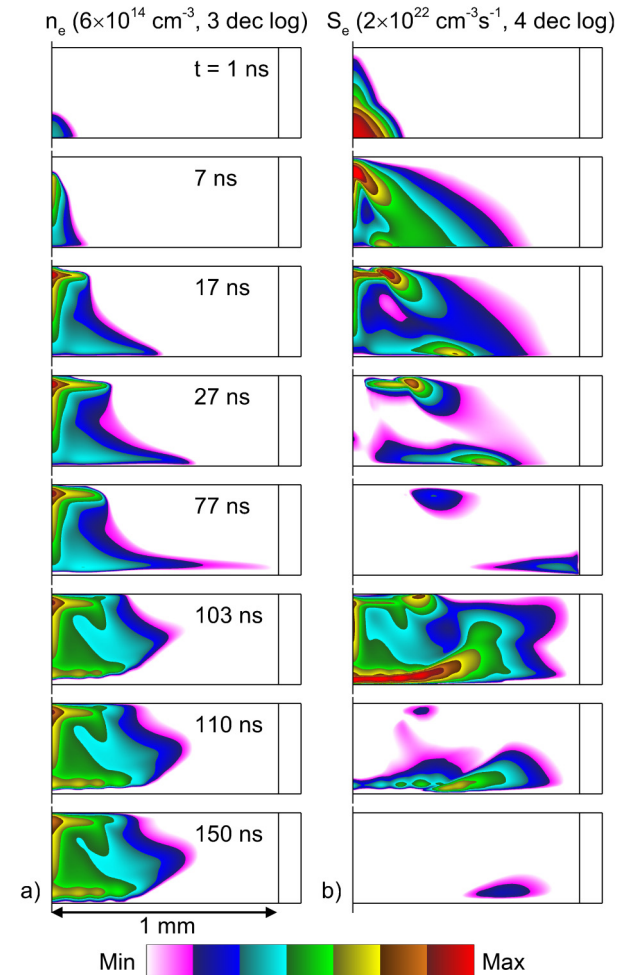
FIG. 5. Plasma properties during the voltage pulse. (a) Electron density and (b) electron-impact ionization source. The images are plotted on a log-scale with the maximum value indicated.

pulse. These photon fluxes represent the instantaneous magnitude of photons passing through a given point regardless of direction. This is the magnitude of the flux that would, for example, photoionize an atom at a given location. Since the plasma streamer is largely on the axis (left boundary in these images), the general direction of the photon propagation is left-to-right. The local maxima in flux reflect local maxima in the density of emitters, as the local flux from any emitter scales as $1/r^2$ (r being distance from the emitter). When summing over emitters at the distance of the PCS, the fluxes originating from non-uniform emitters produce a fairly uniform fluence.

The photon fluxes are as large as several times 10^{17} cm^{-2} s^{-1}, which corresponds to a power flux of about 0.5–1 W/cm^2. The photon flux due to the He(3P) $\rightarrow$ He transition increases quickly, in response to an increasing electron density and T_e, reaching a
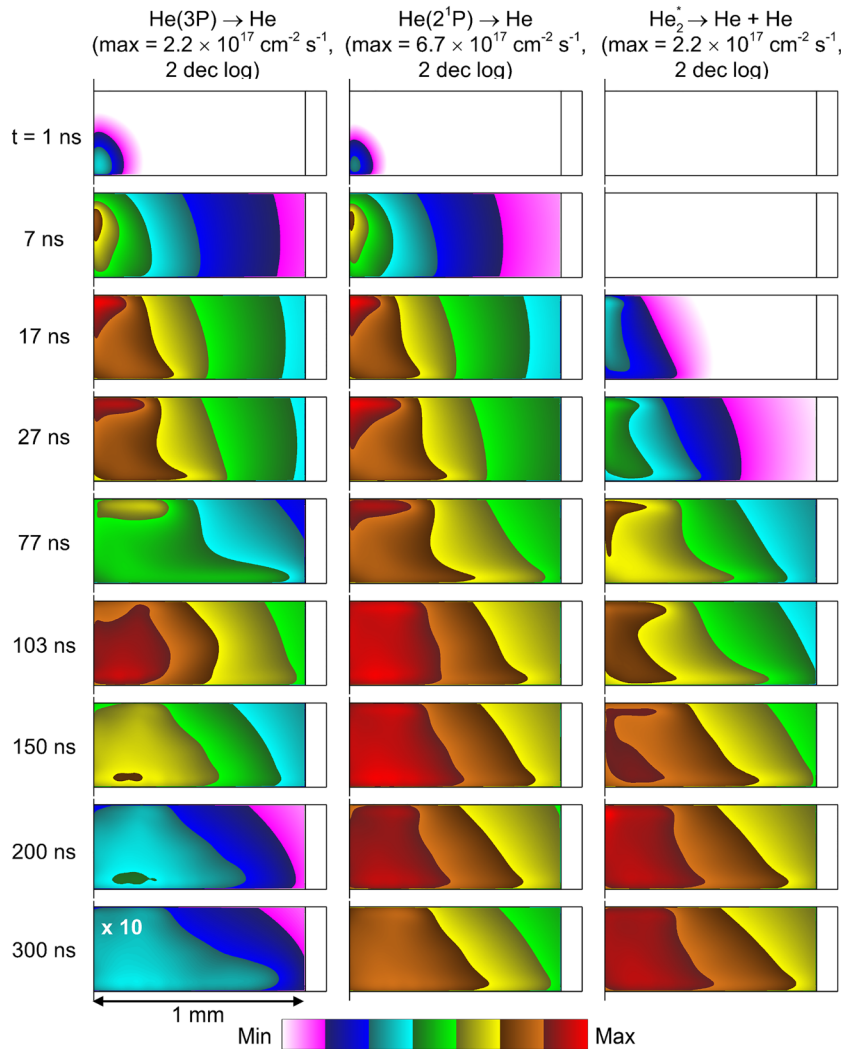
FIG. 6. Photon flux from He(3P), He(2^1P), and He$_2$* over the pulse and afterglow. Note that emission from He(3P) for 300 ns has been multiplied by a factor of 10.

maximum at 17 ns. After 17 ns, the photon flux decreases substantially, indicating that He(3P) has a short lifetime compared to the pulse length and its depletion by Penning reactions and conversion to He$_2$*. At 103 ns, the photon flux again increases just after the voltage falls, corresponding to the increase in the electron density at this time due to the reverse IW propagation on the fall of the pulse. At 150 ns, the photon flux again decreases due to the short lifetime of He(3P), Penning reactions, and its conversion to He$_2$*. At later times, the flux decays to small values as the He(3P) density decreases.

The photon flux from He(2^1P) → He follows similar trends as the photon flux from He(3P) → He. However, He(2^1P) has a longer lifetime than He(3P), as shown by a smaller decrease in the photon flux during and after the pulse. While He(3P) and He(2^1P) are both consumed in Penning ionization processes and formation of He$_2$* with the same rate coefficients, He(3P) also decays by

radiative transitions that are not trapped,

$$\text{He}(3P) \rightarrow \text{He}(2^3S)(9.47 \times 10^6 \text{ s}^{-1}), \quad (5)$$

$$\text{He}(3P) \rightarrow \text{He}(2^1S)(1.34 \times 10^7 \text{ s}^{-1}). \quad (6)$$

These two reactions result in a more rapid decrease in the density of He(3P) compared to He(2^1P), leading to a smaller decrease in photon flux during and after the pulse from He(2^1P) compared to He(3P). The photon flux from He(2^1P) reaches its maximum at 147 ns and decreases after 147 ns. The density of He(2^1P) is also maintained by electron collisional transfer from the longer lived He metastable states.

The photon flux from He$_2$* → He + He does not follow the trends of He(3P) and He(2^1P). Rather, the photon flux continually
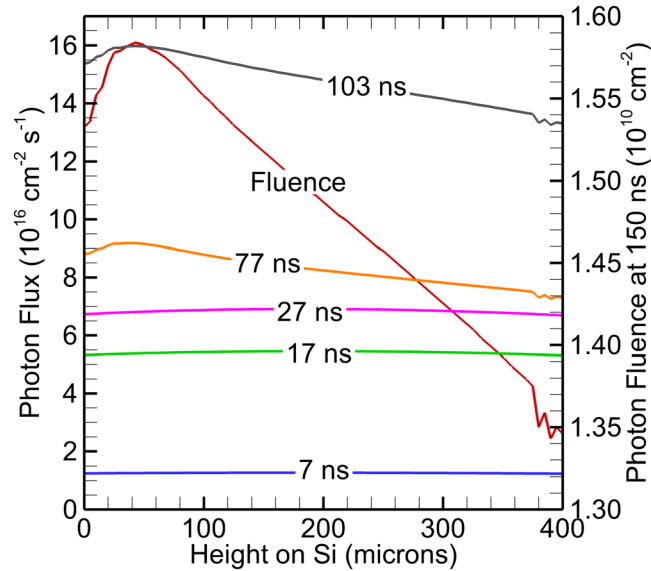
FIG. 7. Photon flux at different times during the pulse and photon fluence to the Si at 150 ns.

FIG. 8. Electron density and total photon flux at 150 ns for different capacitances.

increases throughout the 150 ns in spite of He_2^* having the largest rate of emission. The cause is that He_2^* takes longer to form than either $He(3P)$ and $He(2^1P)$. The formation of He_2^* occurs by a three-body reaction, $He^* + He + M \rightarrow He_2^* + M$, where He^* is an excited He state and M is a third body. (In this mixture, the third body is dominantly another He atom.) The density of He_2^* increases only after there are appreciable densities of excited He, and the source of He_2^* persists even after T_e decreases as He^* is consumed in He_2^* production. He excited states are also formed after T_e decreases by the dissociative recombination of He_2^+. Over $3\,\mu s$ was simulated in the base case to determine when the photon flux from He_2^* decreases. The photon flux from He_2^* reaches a maximum near 200 ns, after the voltage pulse has terminated.

The total photon flux (sum of the three photon fluxes) during the pulse onto the PCS is shown in Fig. 7, as well as the photon fluence over 150 ns. The total photon flux increases over the duration of the pulse. While the photon flux from $He(3P)$ is strongly modulated during the plasma pulse, the photon fluxes from He (2^1P) and He_2^* remain high during and after the pulse. The photon flux through 27 ns is relatively uniform across the PCS. At later times, the photon flux has a maximum at the bottom of the PCS, corresponding to the spreading of the surface ionization wave on the bottom dielectric. As a result, the fluence of photons also exhibits a small maximum near the bottom of the PCS but varies by less than 20% over the surface.

IV. CAPACITANCE OF THE DIELECTRIC

The specific capacitance C (F/cm^2) is proportional to ε_r and inversely proportional to d, the thickness of the dielectric between the plasma and electrode. The simulated electron density and total
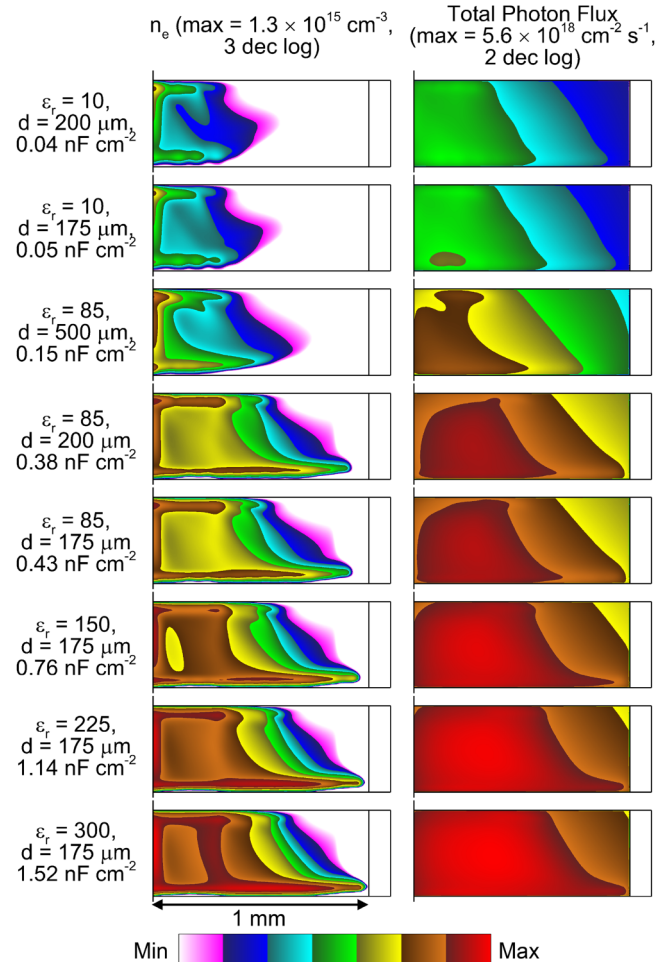
photon flux are shown at 150 ns in Fig. 8 for C varying from 0.04 to 1.52 nF/cm^2. These values were produced by combinations of varying both ε_r (10–300) and d (175–500 μm). As C increases, the electron density and total photon flux both increase in magnitude. From a circuit perspective, the RC time constant (R being the effective resistance of the plasma) to charge the capacitance of the dielectric due to collecting charged particle current also increases. With there being less voltage dropped across the dielectric and more voltage dropped across the plasma gap, there is a larger electric field in the plasma. The larger electric field sustained for a longer period produces a large electron density and photon flux. Larger capacitance also implies larger energy deposition per pulse and, therefore, higher rates of gas heating and device heating. The energy deposition occurring during the single pulses addressed here produces nominal device heating. The pulse repetition frequency (PRF) will then determine the average power dissipation and device heating.

In addition to the increased magnitude of the electron density on the axis, the electron density also spreads further along the top and bottom dielectrics as C increases. An increase in C leads to an increase in the charge on the dielectric, which increases the parallel component of the electric field, leading to more spreading of the SIW. The longer charging time with larger C simply enables the SIW more time to spread. The additional spreading of the SIW enables more excited states of He to be generated closer to the PCS, therefore increasing the total photon flux to the PCS. The average photon fluence and relative efficiency (fluence/energy deposition) to the PCS at 150 ns are shown in Fig. 9 for the different values of C. In spite of the variation in the capacitance resulting from varying both ε_r and d, the maximum in photon fluence increases somewhat linearly with increasing C, while the efficiency generally decreases with increasing C. The decrease in efficiency results from the longer current pulse length with larger capacitance, which occurs at lower voltage and electric field across the gap. The lower electric field produces a lower electron temperature and less efficient production of excited states. The deviation from linearity is a result of the capacitances being varied by using different combinations of dielectric permittivity and thickness, and from the decrease in efficiency. The anomalously low efficiencies result from using thicker dielectric, which makes the electrodes look less planar to the plasma.

Since the photoionization is typically not saturating the signal, a linear increase in the photon fluence due to an increase in the capacitance will produce a linear increase in the ion current. Assuming that there is no other source of noise, and the PID signal remains electronically stable, then the detector would be shot-noise limited. If so, as the signal (or fluence of the VUV photons) increases, then the noise increases by the square root of the VUV photon fluence. As a result, signal-to-noise will increase with increasing photon fluence. However, from a practical perspective, other sources of noise are typically larger than shot-noise. For example, electromagnetic interference (EMI) noise in pulsed discharge devices typically occurs during the high voltage breakdown phase. Since with a constant voltage, the breakdown phase of device operation is essentially the same independent of capacitance, one would expect the noise level to be relatively constant as a function of capacitance. For these conditions, signal-to-noise should increase with increasing capacitance and increasing photon fluence.

V. ELECTRODE CONFIGURATION

The most direct optimization of the electrode configuration is laterally moving the electrode toward the PCS, as shown in Fig. 4. In this configuration, the electron density and total photon flux do not significantly vary between different electrode positions, aside from their maximum being shifted to under the electrodes. With the electrode located immediately adjacent to the PCS, the spreading of the SIW on the top and bottom surfaces is interrupted by the PCS itself. The average fluences to the PCS at 150 ns and relative efficiency (fluence/energy deposition) are shown in Fig. 10 as a function of distance from the center of the electrode to the PCS. As the distance to the PCS decreases, the photon fluence linearly increases. This increase reflects the PCS subtending, on average, a larger solid angle for collecting isotropically emitted photons from streamers that are closer to the PCS. In a 2D geometry, thin plasma streamers appear to be planes, which, in principle, should produce uniform photon fluxes perpendicular to the plane. In this case, the fluence onto the PCS should be nearly independent of distance.
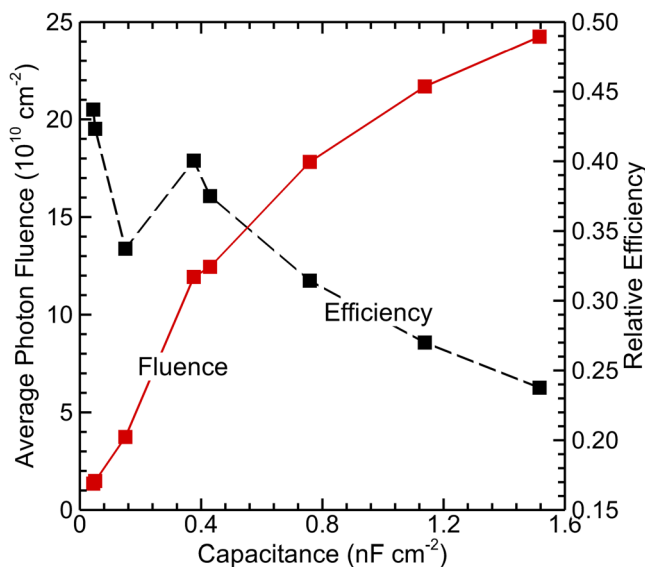

FIG. 9. Average fluence to the PCS at 150 ns and relative efficiencies for different capacitances. The capacitances were varied by using different combinations of dielectric thickness and permittivity.
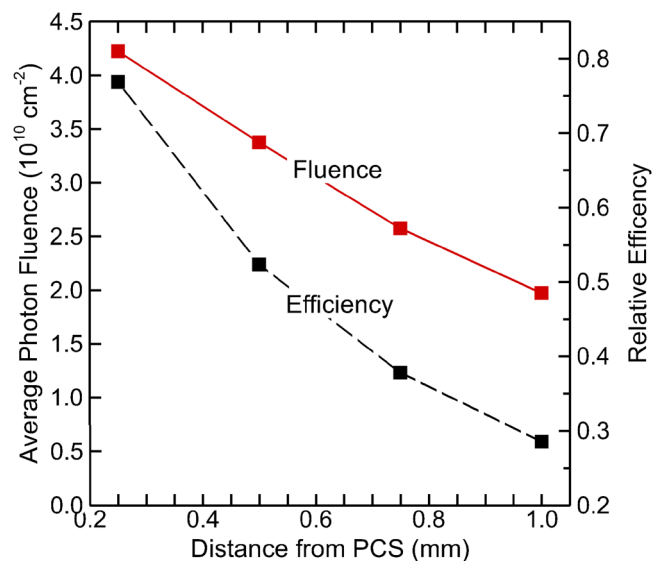

FIG. 10. Average photon fluence to the PCS and relative efficiency at 150 ns for different distances from the center of the electrode to the PCS in the full reactor geometry.

09 April 2024 11:30:17

The increase in the photon fluence indicates that photons are being dominantly produced by sources that appear to be more point-like than plane-like. The relative efficiency increases with electrodes positioned closer to the PCS largely for this reason. In spite of the increase in the fluence and efficiency, the energy deposition decreases with electrodes placed closer to the PCS (by approximately 20% from 1 to 0.2 mm). This decrease in energy deposition
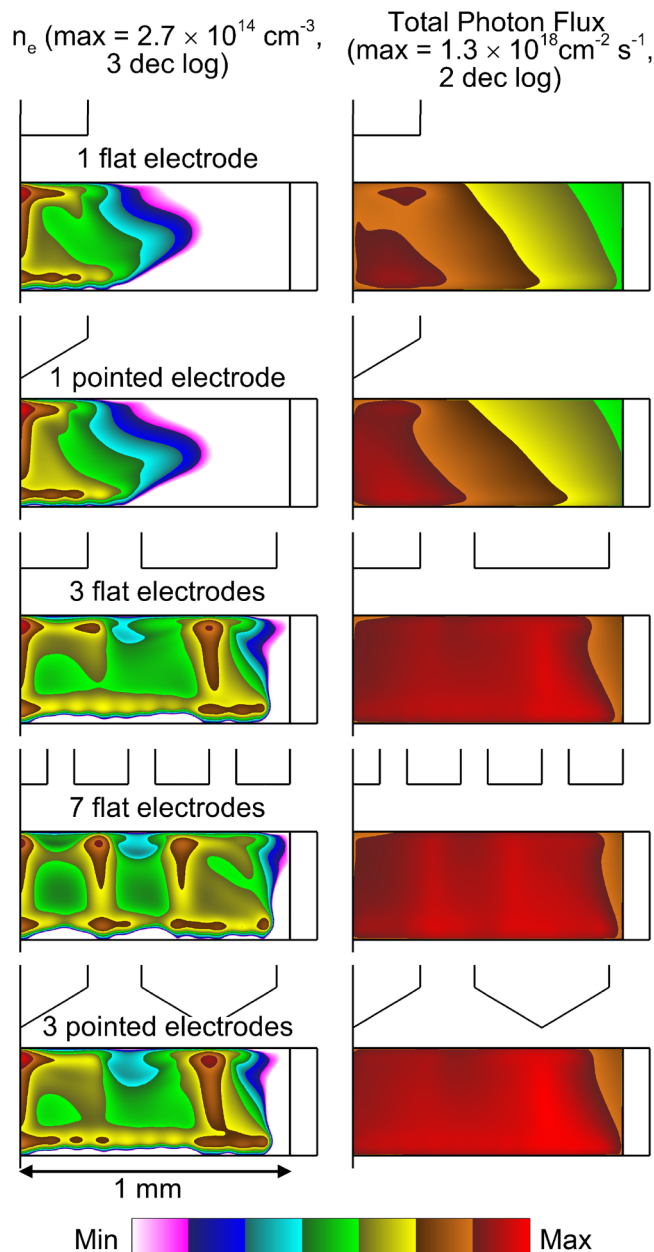
is in part due to the interruption of the surface ionization waves along the top and bottom surfaces by the proximity of the PCS.

The configuration of the electrodes also affects the photon flux to the PCS as a result of electric field enhancement in addition to proximity to the PCS. The simulated electron density and photon flux for different electrode configurations (described in Fig. 3) are shown in Fig. 11 at 150 ns. The images in Fig. 11 are of half of the device (with a reflective boundary condition on the left side). The electrode configurations are one flat electrode, one pointed electrode, three flat electrodes (the image shows half the center electrode and the full electrode on the right side), seven flat electrodes, and three-pointed electrodes. A streamer was initiated beneath each electrode by providing seed electrons. The average fluences to the PCS and relative energy efficiency at 150 ns are shown in Fig. 12 for these electrode configurations.

Comparing the single flat and pointed electrodes, the pointed electrode produces a marginally larger electron density and total photon flux as the pointed electrode enhances the electric field in the plasma. However, since the capacitance of the flat and pointed electrodes is not significantly different, the maximum fluence produced by the two electrodes is not significantly different. With three and seven flat electrodes, the electron densities beneath each electrode are similar. However, with individual contributions from each of the streamers, the total photon flux and fluence to the PCS increases. Each individual streamer produces SIWs that propagate both left and right on the dielectric surfaces. With there being multiple streamers producing SIWs propagating in both directions, SIWs intersect with the SIW launched by a neighboring streamer.
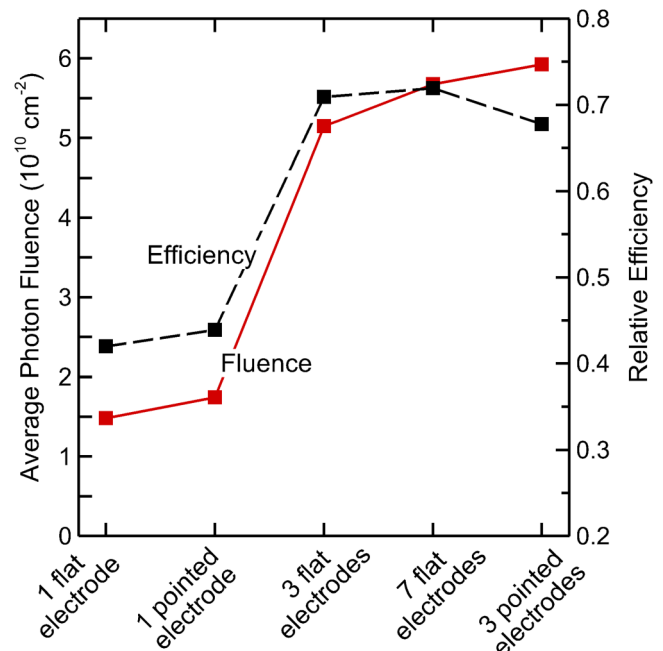

FIG. 11. Electron density and total photon flux at 150 ns for different electrode configurations.

FIG. 12. Average photon fluence to the PCS and relative efficiency at 150 ns for different electrode configurations.

The interference of these intersecting SIW produces coherent structures, such as the periodic maxima in the electron density.

Proximity effects aside, if the streamers produced by multiple electrodes equally contributed to the fluence collected by the PCS, the total fluence would simply scale with the number of electrodes. When adding electrodes, half of the added electrodes are close to the PCS and half are further away. The average fluence produced by three flat electrodes is $5.2 \times 10^{10} \, \text{cm}^{-2}$, whereas the fluence collected when operating with a single electrode is $1.5 \times 10^{10} \, \text{cm}^{-2}$. The three-electrode configuration is about 15% more productive per electrode in generating photon fluence. The advantage of adding electrodes diminishes for the seven flat electrode configuration. Although the total fluence is larger ($5.7 \times 10^{10} \, \text{cm}^{-2}$), the per-streamer productivity is lower by about 50%. The maximum photon fluence is produced by the three-pointed electrode configuration, which is about 15% more productive per electrode in generating photon fluence compared to the single pointed electrode.

The increase in the fluence with the multi-electron configurations is also a result of increasing efficiency (fluence/energy deposition). This increase in efficiency is largely a consequence of the arrays of electrodes having closer proximity to the PCS and so subtending a larger collection angle.

VI. CONCLUDING REMARKS

Scaling properties were discussed using results from simulations for a miniature photoionization detector (PID) based on photons produced in a dielectric barrier discharge sustained in He with N_2 and O_2 impurities—a He dielectric barrier discharge PID (HDBD-PID). The VUV flux producing ionization of the analyte is produced by atomic excited states [He(2^1P), He(3P)] and excimer He_2^* emission. The plasma properties, VUV photon flux, and VUV photon fluence in the PID were examined over one 100 ns voltage pulse and afterglow using the 2D plasma hydrodynamics model *nonPDPSIM*. An IW and corresponding SIW propagated at the rise and fall of the voltage pulse. During the constant voltage portion of the pulse, the electron density is sustained by sources of electrons from Penning ionization reactions by excited states of He with N_2 and photoionization of N_2. The photon flux from He(3P) was significantly modulated during the voltage pulse, increasing as the voltage increased and decreased, the times at which ionization waves are launched. The photon flux from He(2^1P) was less modulated during the pulse, as He(2^1P) has a longer lifetime than He(3P). The photon flux from He_2^* continued after the voltage pulse until 200 ns, as He_2^* is repopulated by three-body reactions involving atomic excited states of He. The total photon flux and fluence to the analyte inlet varied by less than 20% across the height of the analyte inlet. The predicted dynamics of the spectrum of photon emission provides opportunities for experimental validation by time resolved spectroscopy.

The electrode configuration and capacitance of the dielectric were varied with the goal of maximizing the total photon fluence to the analyte. Higher photon fluences to the analyte were produced by using pointed electrodes, arrays of electrodes, and positioning the electrodes close to the PCS. However, the most strategic method to increasing photon fluence is to increase the capacitance of the dielectric between the plasma and electrodes. In this work, the dependence of photon fluence on electrode configurations and capacitance was examined independently. However, using a high capacitance dielectric combined with an array of pointed electrodes placed close to the analyte would likely result in a higher photon fluence than either technique individually. While these trends were obtained for the PID operating in He, we expect these trends would hold for other gases, including Ar. Using Ar may be a more economical choice for PID operation despite its lower photon energies. Although not investigated here, the upper limit to increasing photon fluence with high repetition rate operation is likely not the physics of the photon-producing plasma but rather heat dissipation.

Optimizing fluence to the analyte while reducing power consumption is a design goal. Over the range of capacitances investigated, fluence to the analyte generally increases with capacitance. However, the efficiency of delivering those photons generally decreases with increasing capacitance. The most direct way to maximize the fluence is to position the electrode structures as close as possible to the analyte in order to maximize the solid angle of photon emission that maps onto the analyte. That said, one of the original motivations for the development of plasma-based PIDs was to have a physical separation between the plasma and the analyte, while radiation transport delivers the photons to the analyte beyond the bounds of the plasma. Having the plasma in contact with the analyte would result in electron and ion impact dissociation of the analyte, which would interfere with the selectivity afforded by the photodissociation by the discrete VUV wavelengths. From this perspective, maximizing photon fluence to the analyte by electrode placement will be limited when plasma interactions begin to interfere with the desired selectivity.

AUTHOR DECLARATIONS
Conflict of Interest

Xudong Fan is an inventor of the original helium dielectric barrier discharge photoionization detector (HDBD-PID), which has been licensed to Nanova Environmental, ChromX Health, and RUA Diagnostics.

Author Contributions

Mackenzie Meyer: Data curation (equal); Formal analysis (equal); Investigation (lead); Methodology (equal); Software (equal); Validation (equal); Writing – original draft (lead); Writing – review & editing (equal). **Xiaheng Huang:** Formal analysis (equal); Investigation (equal); Methodology (equal); Writing – review & editing (equal). **Xudong Fan:** Conceptualization (equal); Investigation (equal); Methodology (equal); Project administration (equal); Supervision (equal); Writing – review & editing (equal). **Mark J. Kushner:** Conceptualization (equal); Formal analysis (equal); Funding acquisition (equal); Investigation (equal); Methodology (equal); Project administration (equal); Supervision (equal); Writing – review & editing (equal).

09 April 2024 11:30:17

DATA AVAILABILITY

The data that support the findings of this study are contained in the paper and available from the corresponding author upon reasonable request.

REFERENCES

[1] R. Nasreddine, V. Person, C. A. Serra, and S. Le Calvé, Sens. Actuators, B **224**, 159 (2016).

[2] J. C. Soo, E. G. Lee, R. F. LeBouf, M. L. Kashon, W. Chisholm, and M. Harper, J. Occup. Environ. Hyg. **15**, 351 (2018).

[3] S. Narayanan, G. Rice, and M. Agah, Sens. Actuators, B **206**, 190 (2015).

[4] D. W. You, Y. S. Seon, Y. Jang, J. Bang, J. S. Oh, and K. W. Jung, J. Chromatogr. A **1625**, 461267 (2020).

[5] G. C. Rezende, S. L. Calvé, J. J. Brandner, and D. Newport, Sens. Actuators, B **287**, 86 (2019).

[6] X. Huang, R. Sharma, A. D. Sivakumar, S. Yang, and X. Fan, Anal. Chem. **95**, 8496 (2023).

[7] S. Narayanan, M. Agah, and G. Rice, in *Proceedings of IEEE Sensors* (IEEE, 2013), p. 51.

[8] M. Akbar, M. Restaino, and M. Agah, Microsyst. Nanoeng. **1**, 15039 (2015).

[9] M. Akbar, H. Shakeel, and M. Agah, Lab Chip **15**, 1748 (2015).

[10] H. Zhu, M. Zhou, J. Lee, R. Nidetz, K. Kurabayashi, and X. Fan, Anal. Chem. **88**, 8780 (2016).

[11] M. W. Li, A. Ghosh, R. Sharma, H. Zhu, and X. Fan, Sens. Actuators, B **332**, 129504 (2021).

[12] H. Cai and S. D. Stearns, J. Chromatogr. A **1284**, 163 (2013).

[13] C. F. Poole, J. Chromatogr. A **1421**, 137 (2015).

[14] S. A. Norberg, E. Johnsen, and M. J. Kushner, Plasma Sources Sci. Technol. **24**, 035026 (2015).

[15] A. Fridman and L. A. Kennedy, *Plasma Physics and Engineering* (CRC Press, 2011).

[16] W. Van Gaens and A. Bogaerts, J. Phys. D: Appl. Phys **46**, 275201 (2013).

[17] S. Norberg, "Modeling atmospheric pressure plasma jets: Plasma dynamics, interaction with dielectric surfaces, liquid layers and cells," Ph.D. thesis (University of Michigan, 2015).

[18] F. Emmert, H. H. Angermann, R. Dux, and H. Langhoff, J. Phys. D: Appl. Phys. **21**, 667 (1988).

[19] P. Kurunczi, J. Lopez, H. Shah, and K. Becker, Int. J. Mass Spectrom. **205**, 277 (2001).

[20] A. M. Lietz, E. V. Barnat, J. E. Foster, and M. J. Kushner, J. Appl. Phys. **128**, 083301 (2020).

[21] J. W. Gallagher, C. E. Brion, J. A. R. Samson, and P. W. Langhoff, J. Phys. Chem. Ref. Data **17**, 9 (1988).

09 April 2024 11:30:17